Nuclear high-ionisation outflow in the Compton-thick AGN NGC 6552 as seen by the JWST mid-infrared instrument

Álvarez-Márquez, J.; Labiano, A.; Guillard, P.; Dicken, D.; Argyriou, I.; Patapis, P.; Kavanagh, P. J.; Alberts, S.; Brandl, B. R.; More Authors

DOI
10.1051/0004-6361/202244880

Publication date
2023

Document Version
Final published version

Published in
Astronomy and Astrophysics

A&A 672, A108 (2023)
https://doi.org/10.1051/0004-6361/202244880

Astronomy & Astrophysics

Nuclear high-ionisation outflow in the Compton-thick AGN NGC 6552 as seen by the JWST mid-infrared instrument

J. Álvarez-Márquez[1], A. Labiano[2,1], P. Guillard[3,4], D. Dicken[5], I. Argyriou[6], P. Patapis[7], D. R. Law[8], P. J. Kavanagh[9], K. L. Larson[10], D. Gasman[6], M. Mueller[11,12], S. Alberts[13], B. R. Brandl[14,15], L. Colina[1], M. García-Marín[16], O. C. Jones[5], A. Noriega-Crespo[8], I. Shivaei[13], T. Temim[17], and G. S. Wright[5]

[1] Centro de Astrobiología (CAB), CSIC-INTA, Carretera de Ajalvir km4, 28850 Torrejón de Ardoz, Madrid, Spain
e-mail: javier.alvarez@cab.inta-csic.es
[2] Telespazio UK for the European Space Agency (ESA), ESAC, Camino Bajo del Castillo s/n, 28692 Villanueva de la Cañada, Spain
[3] Sorbonne Université, CNRS, UMR 7095, Institut d'Astrophysique de Paris, 98bis Bd Arago, 75014 Paris, France
[4] Institut Universitaire de France, Ministère de l'Enseignement Supérieur et de la Recherche, 1 rue Descartes, 75231 Paris Cedex 05, France
[5] UK Astronomy Technology Centre, Royal Observatory Edinburgh, Blackford Hill, Edinburgh EH9 3HJ, UK
[6] Institute of Astronomy, KU Leuven, Celestijnenlaan 200D bus 2401, 3001 Leuven, Belgium
[7] Institute for Particle Physics and Astrophysics, ETH Zurich, Wolfgang-Pauli-Str 27, 8093 Zurich, Switzerland
[8] Space Telescope Science Institute, 3700 San Martin Drive, Baltimore, MD 21218, USA
[9] Dublin Institute for Advanced Studies, Astronomy & Astrophysics Section, 31 Fitzwilliam Place, Dublin 2, Ireland
[10] AURA for the European Space Agency, Space Telescope Science Institute, 3700 San Martin Drive, Baltimore, MD 21218, USA
[11] Kapteyn Astronomical Institute, University of Groningen, PO Box 800, 9700 AV Groningen, The Netherlands
[12] SRON Netherlands Institute for Space Research, Postbus 800, 9700 AV Groningen, The Netherlands
[13] Steward Observatory, University of Arizona, 933 N. Cherry, Tucson, AZ 85721, USA
[14] Leiden Observatory, Leiden University, PO Box 9513, 2300 RA Leiden, The Netherlands
[15] Faculty of Aerospace Engineering, Delft University of Technology, Kluyverweg 1, 2629 HS Delft, The Netherlands
[16] European Space Agency, Space Telescope Science Institute, Baltimore, MD, USA
[17] Princeton University, 4 Ivy Ln, Princeton, NJ 08544, USA

Received 4 September 2022 / Accepted 8 February 2023

ABSTRACT

Context. During the commissioning of the *James Webb* Space Telescope (JWST), the mid-infrared instrument (MIRI) observed NGC 6552 with the MIRI Imager and the Medium-Resolution Spectrograph (MRS). NGC 6552 is an active galactic nucleus (AGN) at a redshift of 0.0266 (D_L = 120 Mpc) classified as a Seyfert 2 nucleus in the optical and Compton-thick AGN in the X-ray.
Aims. This work exemplifies and demonstrates the MRS capabilities to study the mid-infrared (mid-IR) spectra and characterise the physical conditions and kinematics of the ionised and molecular gas in the nuclear regions of nearby galaxies.
Methods. MIRI Imager observations covers the full NGC 6552 galaxy at 5.6 μm. MRS observations covers its nuclear region (3.6×4.3 kpc at 17.7–27.9 μm) in a wavelength range between 4.9 and 27.9 μm. These observations were obtained with the aim to investigate the persistence of the MIRI detectors (residual signal left from previous bright source observations). However, NGC 6552 observations demonstrate the performance and power of the MIRI instrument even with a non-optimal observational strategy.
Results. We obtained the nuclear, circumnuclear, and central mid-IR spectra of NGC 6552. They provide the first clear observational evidence for a nuclear outflow in NGC 6552. The outflow contributes to 67±7% of the total line flux independent of the ionisation potential (27–187 eV) and critical densities (10^4–4×10^6 cm^{-3}), showing an average blue-shifted peak velocity of -127 ± 45 km s^{-1} and an outflow maximal velocity of 698 ± 80 km s^{-1}. Since the mid-IR photons penetrate dusty regions as efficiently as X-ray keV photons, we interpret these results as the evidence for a highly ionised, non-stratified, AGN-powered, and fast outflowing gas in a low density environment (few 10^3 cm^{-3}) located very close (<0.2 kpc) to the Compton-thick AGN. Nine pure rotational molecular Hydrogen lines are detected and spectrally resolved, and exhibit symmetric Gaussian profiles, consistent with the galactic rotation, and with no evidence of outflowing H_2 material. We detect a warm H_2 mass of $1.9 \pm 1.1 \times 10^7$ $M_\odot$ in the central region (1.8 kpc in diameter) of the galaxy, with almost 30% of that mass in the circumnuclear region. Line ratios confirm that NGC 6552 has a Seyfert nucleus with a black hole mass estimated in the range of 0.6–6 million solar masses.
Conclusions. This work demonstrates the power of the newly commissioned MIRI Medium Resolution Spectrograph to reveal new insights in the kinematics and ionisation state of the interstellar medium around the dusty nuclear regions of nearby active galaxies.

Key words. instrumentation: spectrographs – instrumentation: high angular resolution – galaxies: active – galaxies: Seyfert – galaxies: ISM – galaxies: kinematics and dynamics

1. Introduction

The Mid-Infrared Instrument (MIRI, Rieke et al. 2015b; Wright et al. 2015) on board the *James Webb* Space Telescope (JWST) includes imaging and medium-resolution integral field spectroscopy (IFS) observing modes from 4.9 to 27.9 μm. The MIRI Imager provides sub-arcsec resolution (0.2–0.8 arcsec) images in nine filters, with a clear field of view (FoV)

up to 2.3 square arcmin (Bouchet et al. 2015). The Medium Resolution Spectrometer (MRS) provides IFS in twelve individual spectral bands, organised in four channels (1, 2, 3, and 4) and each of them is divided in three bands (SHORT, MEDIUM, and LONG). The MRS provides a factor of ×10–100 increased sensitivity from previous mid-infrared (mid-IR) telescopes, combined with a sub-arcsec resolution (0.3–0.9 arcsec) in a FoV ranging from ∼13 to ∼56 square arcsec, and a spectral resolution of 75–200 km s^{-1} (Wells et al. 2015; Glasse et al. 2015; Labiano et al. 2021; Jones et al. 2023; Argyriou et al., in prep.). Due to the low central extinction in the mid-IR spectral range, similar to that in the several keV X-ray range (Corrales et al. 2016), and the improvements in the spatial and spectral resolution from previous mid-IR instruments, MIRI will be a key instrument in providing a view into the inner dust-enshrouded nuclear regions of nearby galaxies and offering the possibility of separating the nucleus from its circumnuclear environment and studying both components with unprecedented detail and sensitivity.

Galactic winds and outflows are an universal phenomenon associated with AGNs and star-forming galaxies (Veilleux et al. 2005, 2020; Fabian 2012; King & Pounds 2015). They have been detected in different phases of the gas, from highly ionised to ionised, neutral, and molecular gas, and at both low-z and high-z (Rodríguez-Ardila et al. 2006; Guillard et al. 2012; Veilleux et al. 2013; Arribas et al. 2014; Harrison et al. 2016; Emonts et al. 2017; Pereira-Santaella et al. 2018; Davies et al. 2020; Spilker et al. 2020; Álvarez-Márquez et al. 2021). The mid-IR wavelength range is very rich in coronal emission lines, that is, lines with ionisation potential ($E^*_{\rm ion}$) that is close or above 100 eV, of different elements (sulfur, neon, iron, argon, magnesium, among others). These lines, together with the low extinction in this spectral range relative to the optical, provide a unique opportunity to probe the gas close to the AGN and therefore to establish the physical conditions and kinematics of the outflows in the inner regions close to the black hole and accreting torus (e.g., Pereira-Santaella et al. 2010; Fischer et al. 2011).

NGC 6552 is a galaxy located at a luminosity distance ($D_{\rm L}$) of 120 Mpc (z = 0.02656±0.00042) that is classified as an active galactic nucleus (AGN) Seyfert 2 in the optical (Moran et al. 1996; Bower et al. 1996; Falco et al. 1999; Paturel et al. 2002; Gioia et al. 2003; Shu et al. 2007), as well as a Compton-thick AGN (CT-AGN), with a derived column density of $\log(N_{\rm H})$ = 24.05 cm^{-3}, in the X-ray (Ricci et al. 2015). The most recent X-ray studies with *XMM-Newton* (Jansen et al. 2001), complemented with *NuSTAR* (Harrison et al. 2013) observations sensitive to hard X-rays in the 3–78 keV range, have confirmed the classification of NGC 6552 as a CT-AGN (Torres-Albà et al. 2021). The X-ray model predicts the presence of a CT-AGN within a Compton-thin torus oriented nearly edge-on, at 75 deg with respect to our line of sight (Torres-Albà et al. 2021). NGC 6552 has also been observed in imaging and spectroscopy at mid-IR wavelengths with *Spitzer* and WISE. These observations have been used to cross-calibrate the long-wavelength band of WISE (W4) with the *Spitzer* InfraRed Spectrograph long-low module (IRS-LL) and MIPS 24 μm channel (Jarrett et al. 2011).

In this paper, we demonstrate the MIRI capabilities to study the physical conditions and kinematics of the nuclear regions in nearby galaxies, with the example of NGC 6552. The paper is structured as follows: Sect. 2 describes the MIRI Imager and MRS observations of NGC 6552. Sections 3 and 4.1 explains the calibration of the MIRI Imager and MRS data. Section 4.2 shows the final calibrated spectra of NGC 6552. Section 5 presents the fluxes and kinematics measurements of all detected emission lines, the properties of the ionised outflowing gas and the warm molecular hydrogen, and the Seyfert nature of the AGN and black hole mass of NGC 6552. Finally, Sect. 6 summarises and concludes the paper. We have adopted H_0 = 67.7 km s^{-1} Mpc^{-1} and $\Omega_{\rm m}$ = 0.307 (Planck Collaboration XIII 2016) as cosmological parameters. The corresponding luminosity distance ($D_{\rm L}$) and physical scale used in this paper for z = 0.02656 are 120 Mpc and 0.552 kpc arcsec^{-1}, respectively (Wright 2006).

2. Observations

MIRI data of NGC 6552 was obtained on May 7, 2022, during the commissioning of JWST, as part of the persistence characterisation of the MIRI detectors (PID 1039, P.I. D. Dicken). NGC 6552 was selected because is one of the brightest mid-IR source in the northern continuous viewing zone of JWST. Aditionaly, NGC 6552 was used as a calibrator of WISE and *Spitzer*, offering the possibility of cross-checking the MRS absolute photometry.

The aim of this program was to investigate aspects of persistence after long observations of NGC 6552 on the MIRI Imager and MRS detectors and to analyze any artefacts and their decay for up to 25 min. The magnitude of the detector persistence is a function of flux of the source of origin, as well as the time spent observing that source on the same detector pixel (Rieke et al. 2015a). Such persistent behaviour was first measured during MIRI ground testing, so this commissioning activity aimed at verifying that the memory effect seen in the detectors after observing a bright source was as expected.

The program began by taking a background observation with the filter F560W of the MIRI Imager and the MRS observing a star (TYC-4213-1049-1), using the SHORT band (visit 1). The aim of this observation was to gauge the state of the detectors (i.e., to look for any existing artefacts) before the programme started, as well as to use it for background subtraction in the MIRI imager calibration process. A carefully designed sequence of observations followed, using both the MIRI Imager and the MRS simultaneously observing adjacent FoV (see Table 1 for a summary). Visits 2, 3, and 4 were relatively long (555 s) on-target exposures with the MIRI imager aimed at putting a large amount of signal on the detector to see if this imprints a persistence signature on the data. The nucleus of NGC 6552 was able to saturate the imaging data in the third detector readout. Visit 5 was on-target MRS observations with exposure times of 505 s in each of the MRS bands. The MRS observations did not saturate. Visit 6 was used as a reference image and to study persistence decay in the MIRI Imager detector, if any. Finally, MRS observations from visits 2, 3, and 4 have been used for background characterisations purposes.

Since the MRS is spatially undersampled, the MIRI instrument team recommends using four-point dithering[1] on every MIRI observation to maximise the spatial and spectral sampling and the scientific return of the MIRI observations. Due to the nature of this program, the MRS on-target observations did not use dithers, as the programme was designed to investigate artefacts in the detector image rather than on sky. The MIRI Imager visits 2 and 3 used offsets instead of dithers to make sure any persistence artefacts were well separated from one image to another. The MIRI Imager visit 4 uses two four-point, extended dither patterns. The MRS background simultaneous observations

[1] All the details on dithering patterns for the different MIRI modes of observation are available in the JDox MIRI dithering pages.

Table 1. Summary of MIRI commissioning observations for NGC 6552.

Visit (1)	Imager target (2)	MRS target (3)	Imager filter (4)	MRS band (5)	Groups (6)	Int. (7)	Exp. (8)	Dithers (9)	Exp. time [s] (10)
1	Back.	Star	F560W	SHORT	25	1	1	4	277.5
2	NGC 6552	Back.	F560W	SHORT	200	1	1	No dither	555
3	NGC 6552	Back.	F560W	MEDIUM	25	8	1	No dither	574
4	NGC 6552	Back.	F560W	LONG	25	1	1	8	555
5	Back. + Persistence	NGC 6552	F560W	ALL	182	1	1	No dither	3×505
6.1	Back. + Persistence	Back.	F560W	SHORT	25	1	1	4	277.5
6.2	Back. + Persistence	Back.	F2550W	SHORT	25	1	1	4	277.5
6.3	Back. + Persistence	Back.	F560W	SHORT	25	20	1	No dither	1440.2

Notes. Columns describe the visit number of the observation (1), the pointing target for the imager (2) and MRS (3), the filter used in the Imager (4), the band configuration used in the MRS (5), the number of groups (6), integrations (7), exposures (8), and dithers (9) for each observation, as well as the exposure time calculated as 2.77 s × Groups × Int. × Exp. × Dithers (10). Consult PID1039 for details.

(visits 2, 3, and 4) follow the MIRI Imager dither pattern strategies. For additional information on dithers and exposure times see Table 1.

The results of the commissioning investigation demonstrated that the impact of persistence artefacts was very low, where persistence was seen at a level <0.01% of the source flux. Such levels of persistence are easily calibrated using standard MIRI dither patterns and the JWST calibration pipeline. In the case of NGC 6552, the saturating nucleus had no impact on the imaging or subsequent exposures, as the MIRI Imager proved to work extremely well in this relatively high-contrast observation (see Sect. 3).

3. MIRI image

The MIRI imaging data were reprocessed with the v1.6.3 JWST pipeline, using the latest reference files available[2]. After the level 1 detector processing, we applied a fix to the pipeline to re-create rate images averaging only valid data, as a bug in the pipeline affected the pixels that are saturating in after the third group, which is the case for some of the central pixels of NGC 6552. For those pixels, only the first three frames were used. We note that this fix will be implemented in a future version of the pipeline. Then, the level 2 pipeline was run with the default parameters and using the sky flats computed from the LMC data taken during commissioning (PID 1040). These preliminary flats contain image artifacts caused by MIRI reset anomaly (see Ressler et al. 2015, for a discussion of this effects), such as tree-ring shaped structures. However, most of these image artifacts are removed by the master background subtraction (explained below), as the features are stable. Since the calibration of the image is still preliminary, the MIRI Imager data are only used in this paper to illustrate the MRS pointings, crossmatch the MIRI Imager and the MRS photometry, and illustrate the optical quality (in particular the low persistence) and dynamical range of the imager.

A master sky background image was created from the first visit file and subtracted from all the images. This sky image was created by sigma clipping all the images from the visit 1 aligned in instrument coordinates. We note that this injects residual small scale variations at a percent level in the background, which are not critical for our analysis. The left panel Fig. 1 shows on the entire galaxy and the footprints of the MRS channel 4, highlighting the low surface brightness emission in the dusty ring around the barred galaxy. Clumps of star formation are resolved in the bar, the spiral arms and the ring. The right panel shows the central nucleus with the footprints of MRS channels 1, 2, and 3. The MRS footprints are not perfectly centred onto the nucleus because we did not use target acquisition and because those observations were done before updating the distortion model (how the light from the FoV travels through the instrument and gets projected on the detectors) with the flight data of the observatory. The nucleus image exhibits the bright central cross-shaped PSF that is characteristic of the cruciform pattern at this wavelength (Gáspár et al. 2021), which shows that the AGN is dominating the central point-like emission.

4. MIRI spectroscopy

4.1. MRS data calibration

The MRS observations were processed with the JWST calibration pipeline (release 1.8.3). This release uses the build 8.4.2 of the Data Management System (DMS) and context 1017 of the Calibration References Data System (CRDS). The MRS pipeline is divided into three different processing stages (Labiano et al. 2016; Bushouse et al. 2022)[3]. The first stage performs the detector-level corrections, identification, and correction of the cosmic ray (CR) impacts and then transforms the ramps[4] into slope detector products (Morrison et al., in prep.). The second stage assigns the coordinate system, performs the straylight, fringe flat, residual fringe correction, and photometric calibrations to generate fully calibrated individual exposures (Argyriou et al., in prep.). The third stage combines the different dithered exposures to create 3D spectral cubes and 1D extracted spectra (Law et al., in prep.). In the process, it allows for the performance of an outlier rejection and a background matching. The background could be subtracted in stage 2 or 3 of the pipeline depending of the methodology selected by the user. The third stage was not used in this work as the MIRI data were not dithered, and the 1D spectral extraction and background subtraction were performed outside of the JWST calibration pipeline.

We found that the standard pipeline identifies and corrects most of the CR events, but the so-called CR 'showers' and/or high energetic CRs still leave some relevant residual effects even

[2] The version of CRDS was 11.16.6, and CRDS context "jwst_0942.pmap".

[3] Check this JDox page for general information about the JWST calibration pipeline. Review the MIRI Features and Caveats and Pipeline Caveats webpages for the latest status, and information on the MIRI performance and calibration pipeline known issues.

[4] Check this link for the ramp definition in JWST observations.

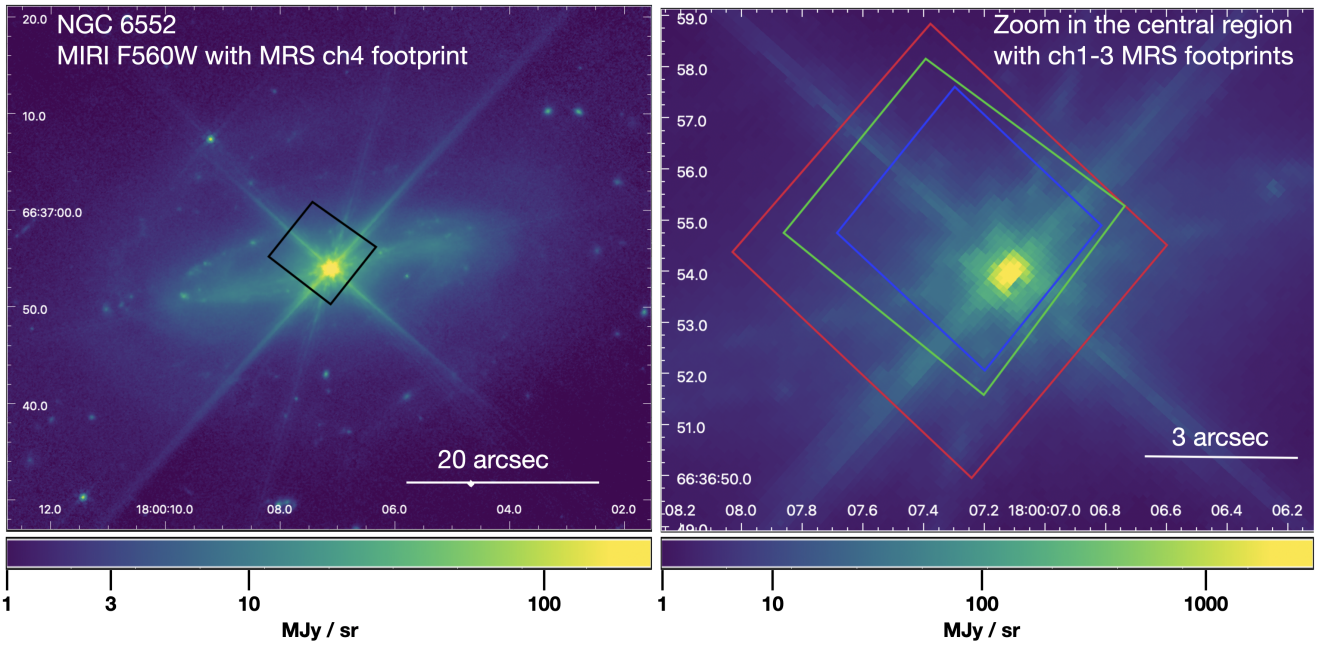

Fig. 1. MIRI background-subtracted images of NGC 6552 in the F560W filter. Left panel shows the entire galaxy (FoV $\sim 20 \times 20$ kpc) and the right panel is a zoom on the central region (FoV $\sim 4 \times 4$ kpc) observed with the MRS. The rectangles show an overlay of the four MRS channels (from the short to long wavelengths: CH1 (FoV = 2×2 pc^2) in blue, CH2 (FoV = 2.6×2.5 pc^2) in green, CH3 (FoV = 3.4×3.4 pc^2) in red on the zoom-in right panel, and CH4 (FoV = 4×4 pc^2) in black on the left panel. Both images are shown on a log-scale, but with different stretches and contrasts to highlight the extended faint ring structure in the left panel, and the point-like central active nuclei in the right panel. The dynamical range in flux between the central pixels and the extended ring is about 20 000, showing the exquisite imaging capabilities of the MIRI detectors.

using the large CRs events function. Also, the current in-flight darks and reset anomaly corrections inject a vertical striping pattern in the slope detector data (see Footnote 3 for examples). Their strength depends on the length of the ramp, where long ramps (>150–200 groups in FASTR1 readout mode, ~500 s) minimise this effect. These effects, along with others such as hot or bad detector pixels, are vastly reduced in four-point dithered observations allowing to obtain the optimal MRS spatial and spectral resolution. The MRS observations of NGC 6552 were taken with no dithers, as the goal of this commissioning activity was not to obtain a final optimised cube. Then, the 3D cubes could still have a small number of spaxels affected by the lack of data due to bad or hot pixels in the detector. These have been identified, masked and interpolated in the 1d extracted spectra presented in Sect. 4.2. We generated 12 3D cubes, that is, one for each of the MRS sub-channels, with spatial sampling of $0.13'' \times 0.13''$, $0.17'' \times 0.17''$, $0.20'' \times 0.20''$, and $0.35'' \times 0.35''$ for channels 1, 2, 3, and 4, respectively.

We extracted the 1D spectra using the 3D cubes and following the standard aperture or annulus photometry (Bradley et al. 2022). We generated three 1D spectra from: (i) a nuclear region, (ii) a circumnuclear region, and (iii) a larger aperture that includes both the nuclear and circumnuclear regions (see Sect. 4.2 for details). All the 1D spectra were derived individually for each of the 12 MRS sub-bands. The background is calculated in an annulus far away of the nuclear and circumnuclear emission of the source and subtracted in the 1D spectra. The extracted 1D spectra are corrected for residual fringing using a post-pipeline spectral-level correction which is a modified version of the detector-level correction available in the JWST calibration pipeline (Gasman et al. 2023; Kavanagh et al., in prep.). The correction reduced the final fringe residuals to levels lower than 6%, and a median level of 2–4% (Rigby et al. 2022). To remove the (minor) flux discontinuities between channels, we stitched the 12 sub-channels together, using the channel 3 bands as a reference. We found that the multiplicative stitching factors needed for each individual channel was lower than ±5% in all sub-channels.

4.2. Spectral extraction

As discussed in Sect. 4.1, the calibrated 3D cubes of NGC 6552 are not optimally sampled because the MRS observations were not dithered. The analysis of this paper has focused in the characterisation of different areas of the central region of NGC 6552, rather than a more complex 2D analysis (e.g., Pereira-Santaella et al. 2022). Even so, the MRS provides an adequate angular resolution to separate the nuclear and circumnuclear regions in NGC 6552. If we assume D_L = 120 Mpc, the MRS point spread function (PSF) full width at half maximum (FWHM) corresponds to physical scales of 170 pc for channel 1 evolving, up to a maximum of 580 pc for channel 4LONG. As an example, Fig. 2 shows the central region of NGC 6552 observed by the MRS channel 1 (3.2×3.7 arcsec). It presents three different line maps illustrating the emission from a coronal line (e.g., [MgV]5.61 μm), a low-excitation line (e.g., [ArII]6.99 μm), and a molecular hydrogen line (e.g., H_2(0-0)S(5)). They show a slightly different morphology between the different species. The coronal emission follows the MRS PSF, which is consistent with an emission coming form the nuclear region. Low-excitation emission is extending beyon the MRS PSF, consistent with the presence of low-excitation emission in the circumnuclear regions of NGC 6552. The molecular hydrogen emission presents a similar morphology to the low-excitation environment in the nuclear an circumnuclear region of NGC 6552, but there is a secondary clump in the NW that is not present in the other species.

We performed three different 1D spectral extraction of the central region of NGC 6552. First, we extracted a spectrum of

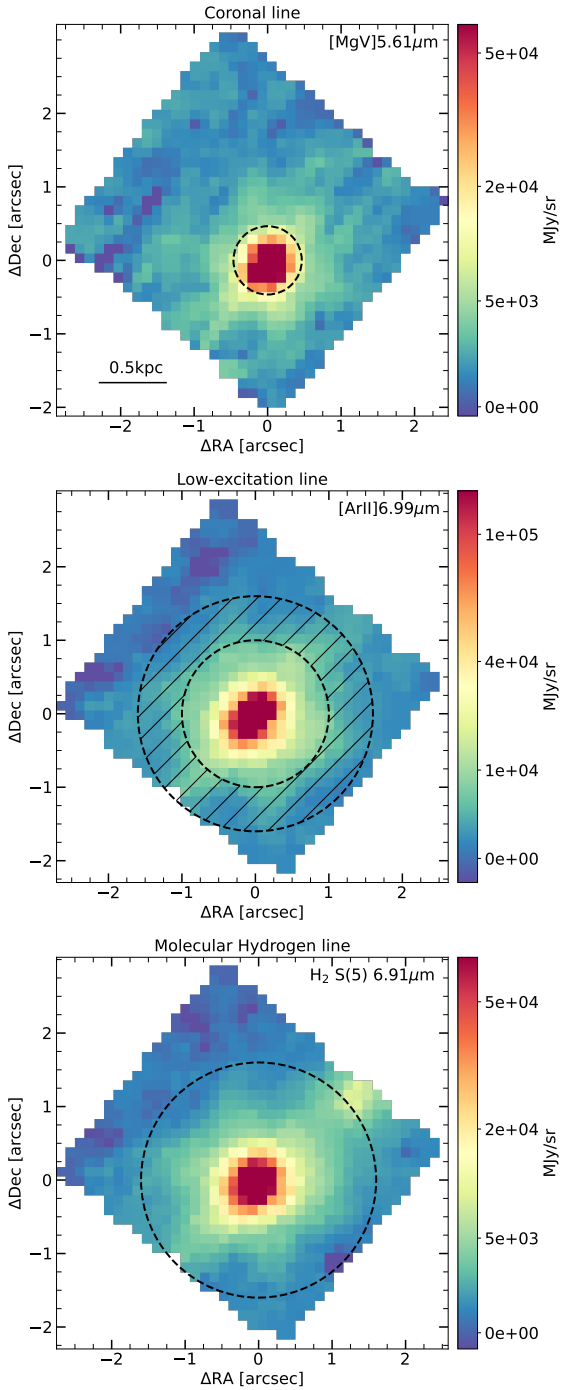

Fig. 2. Emission line maps in the central region of NGC 6552 generated using the MRS channel 1 (3.2 × 3.7 arcsec). Upper panel: line map of [MgV]5.61 μm as a representation of a coronal line emission, and illustrate the aperture used to extract the nuclear spectrum of NGC 6552 in channel 1. Middle panel: line map of [ArII]6.99 μm as a representation of a low-excitation line emission, and illustrate the aperture used to extract the circumnuclear spectrum of NGC 6552. Bottom panel: line map of H_2(0-0)S(5) as a representation of the molecular hydrogen line emission and an illustration of the aperture used to extract the central spectrum of NGC 6552.

the nuclear region using a circular aperture of radius equal to 1.5 × FWHM(λ), where FWHM(λ) = 0.3 arcsec for λ < 8 μm and FWHM(λ) = 0.31 × λ[μm]/8 arcsec for λ > 8 μm (see Fig. 2 upper panel). The selected FWHM (λ) values follow the MRS PSF FWHM and it is the recommended aperture to extract a 1D spectrum of a point-like sources in MRS observations (Law et al., in prep.). We used the MRS PSF models (Patapis et al., in prep.) to correct the aperture losses in the 1D spectra. The percentage of flux that losses out of the selected aperture is 17% for channel 1 and evolves up to 30% in channel 4. Second, we extracted a spectrum of the circumnuclear region in an annulus with an inner radius equal to 1 arcsec, ∼0.55 kpc, and an outer radius of 1.6 arcsec, ∼0.88 kpc (see Fig. 2 middle panel). The inner radius is selected to fit the channel 4 MRS PSF FWHM, which is the minimum distance that allows for the disentanglement of the nuclear and circumnuclear emission in all MRS channels. The outer radius is delimited by the largest aperture allowed by the MRS FoV of channel 1. Based on the MRS PSF models and assuming the nucleus as a point-like source, the circumnuclear region is contaminated by a 2.5%, in channel 1, and up to 12%, in channel 4, of flux coming from the nucleus. We corrected the circumnuclear spectrum from the nuclear contamination by subtracting the percentage of the nuclear emission enclosed in the selected annulus aperture using the nuclear spectrum. Third, we extracted a spectrum (named 'central') in a circular aperture with a constant radius of 1.6 arcsec, ∼0.88 kpc, for all MRS channels (see Fig. 2 bottom panel). The selected radius provides the largest circular aperture allowed by the FoV of the MRS channel 1. Assuming a nuclear emission as a point-like source, a fraction of the nuclear emission will be extended outside of the selected aperture. The percentage of nuclear flux that is lost out of the selected aperture ranges from 6%, in channel 1–20% in channel 4, using the MRS PSF models. We corrected the central spectrum by these flux percentages using the nuclear spectrum. We note that the central spectrum includes the emission of the nuclear and circumnuclear regions, but it is not the sum of both of them.

Figures 3 and 4 show the nuclear, circumnuclear, and central MRS spectra of NGC 6552, and the identification of all emission lines and polycyclic aromatic hydrocarbon (PAH) features. The nuclear and central spectra are dominated by the central AGN emission, which is mainly composed by a steeply rising continuum due to warm dust emission and a large number of high-excitation and coronal emission lines. The spectra also show low-excitation emission lines, warm hydrogen molecular lines, and PAH features from the interplay between the star-formation and the AGN components of NGC 6552. The presence of PAHs indicate that the AGN radiation field has not depleted or destroyed them like seen in other high-luminosity Seyferts (e.g., Alonso-Herrero et al. 2020; García-Bernete et al. 2022). The spectra of the circumnuclear region is mainly dominated by the star-formation component of the galaxy showing low-excitation emission lines, hydrogen molecular lines, and PAH features. However, we found that [NeVI]7.652 μm, [NeV]14.32 μm, and [NeV]24.32 μm coronal emission lines are still present in channels 2, 3 and 4 of the circumnuclear spectrum. The percentage of flux in the circumnuclear spectrum with respect to the nuclear spectrum is 1%, 6%, and 11% (see Table 2), respectively. Therefore, coronal emission lines and some contribution from the continuum coming from the nuclear region of could still be contaminating the circumnuclear spectrum.

The MRS central spectrum and the *Spitzer* IRS-LL low-resolution spectrum (Jarrett et al. 2011) of NGC 6552 agree within ∼5% in channels 3 and 4 (see Fig. 4). Similar results are found in the MIRI commissioning observation of the planetary nebula SMP-LMC-058 for the full MRS wavelength coverage

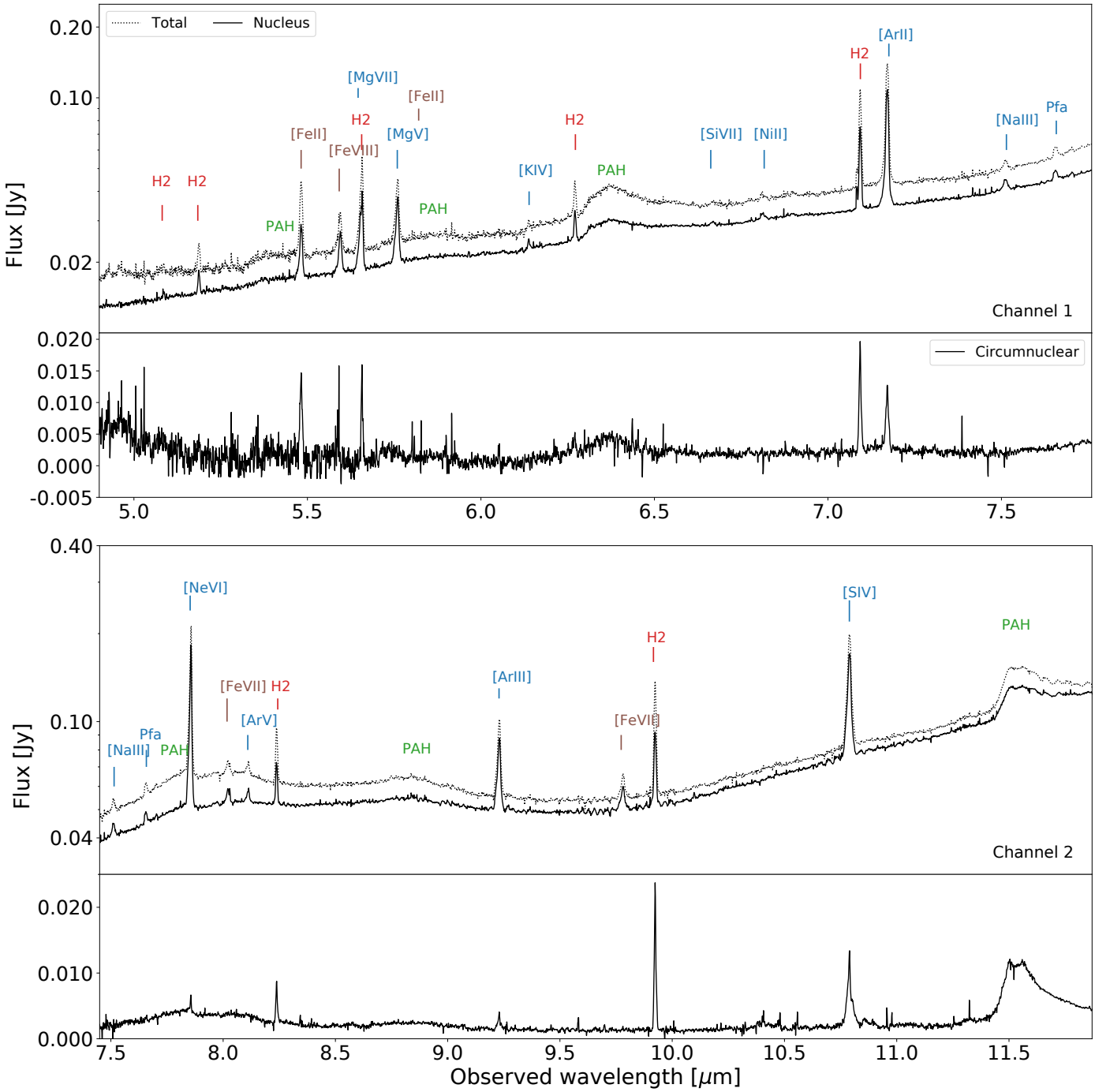

Fig. 3. Nuclear, circumnuclear, and central MRS spectra of NGC 6552 from MRS channels 1 and 2. Upper panel: central and nucleus spectra. Bottom: circumnuclear spectra. The main emission features (listed in Table 2) are highlighted together with the PAHs.

(Jones et al. 2023). The MIRI Imager F560W photometry of the central region, derived from the unsaturated part of the ramps and in a radius of 1.6 arcsec, is 28±3 mJy (see Sect. 3). The equivalent flux for the MRS, taking the central spectra and performing the convolution with the F560W filter transmission curve, is equal to 24±3 mJy. Then, the photometry of the central region agree within 10% for the MIRI Imager F560W image and the MRS channel 1SHORT spectrum. The NGC 6552 calibrated data agree with the statement that the MRS absolute flux uncertainty, based on commissioning data, is $\lesssim$10% (Rigby et al. 2022). Then, we assume a 10% absolute flux errors in deriving line ratios and analysis that follows.

5. Results and discussion

5.1. Emission line fluxes and kinematics

NGC 6552 shows a considerable number of emission lines with high signal-to-noise ratios (S/N) in the nuclear spectrum. We detect all Neon lines present in the mid-IR wavelength range, from [NII] to [NeVI], with S/N between 12 and 80. The presence of coronal atomic lines is evident, going from the brightest ones, with $S/N > 30$, [NeVI]7.65 μm and [NeV]14.32 μm, to shallower ones, with S/N between 20 and 50; that is: [MgVII]5.50 μm, [MgV]5.61 μm, [FeVIII]5.45 μm, or [FeVII]7.82 μm. The same happens with high-excitation atomic lines, that is:

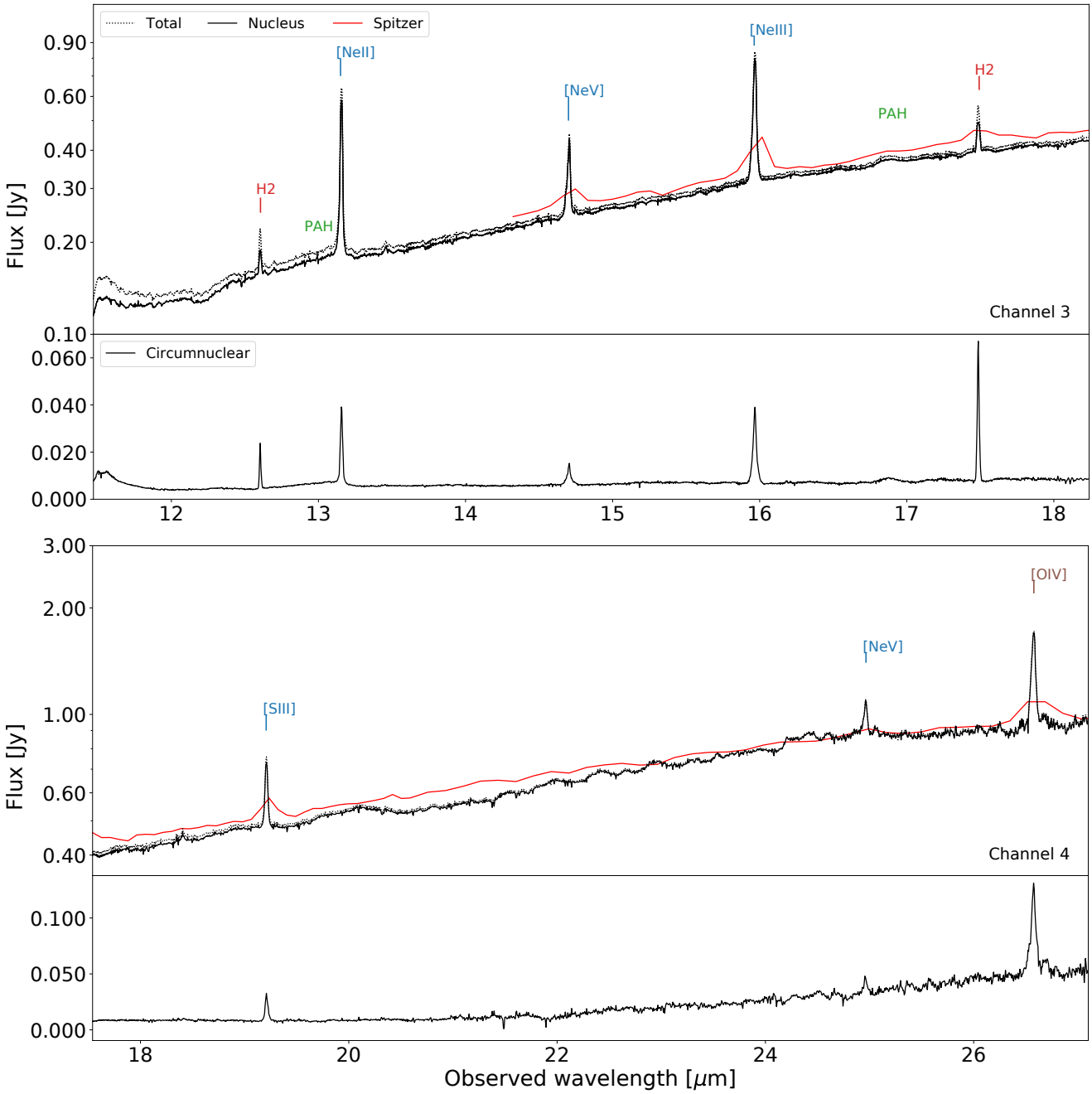

Fig. 4. As Fig. 3, for MRS channels 3 and 4. The MRS channel 4 spectra is shown up to 27 μm due to uncertainties in the photometrical calibrations for $\lambda > 27$ μm. The comparison with the *Spitzer* IRS long low spectrum (red line, from Jarrett et al. 2011) shows excellent photometric agreement from 14.5 to 22 μm (see text for details) and illustrates how the gain in spectral resolution provided by the MRS helps to detect weak PAH features and weak lines (compared to the continuum), in particular, the high-excitation [NeV] lines.

[ArIII]8.99 μm, [SIV]10.51 μm, [OIV]25.89 μm, and low-excitation atomic lines, i.e., [FeII]5.34 μm, [ArII]6.99 μm, [NeII]12.81 μm, [NeIII]15.56 μm and [SIII]18.71 μm, all of them detected with S/N between 30 and 100. The rotational molecular hydrogen lines from the H_2(0-0)S(1) to H_2(0-0)S(8) transitions are detected with S/N between 20 and 50, except for H_2(0-0)S(7) line that is blended with [MgVII]5.50 μm and its S/N drops to 10. We also detected additional emission lines with lower S/N, the most relevant one being Pfund-α, with S/N of ∼14.

We identified and analyzed all detected emission lines with S/N higher than 3 in the NGC 6552 1D extracted spectra. Depending on the line profiles, we performed one-component and two-component Gaussian fit, plus a second-order polynomial to fit the continuum and emission line (Markwardt 2009)[5]. The MRS resolving power ranges from 4000 in channel 1–1500 in channel 4, corresponding to the line FWHM from 75 km s^{-1} to 200 km s^{-1} (Labiano et al. 2021; Jones et al. 2023). The instrumental line broadening was included in the line profile fitting algorithm. The uncertainties on the derived emission line parameters, like the line FWHM, flux, central wavelength, etc, were estimated using a Monte Carlo simulation. The noise of the spectrum was measured as the root mean square (rms) of the

[5] We used the MPFIT Python routine to perform the fits. The version used is available here: https://github.com/segasai/astrolibpy/tree/master/mpfit

Table 2. Fluxes of all detected emission lines in the nuclear, circumnuclear, and central spectra of NGC 6552.

Line	λ_{lab}	$F_{Nuclear}$	$F_{Circum.}$	$F_{central}$
	[μm]	[$\times 10^{-15}$ erg s^{-1} cm^{-2}]		
(1)	(2)	(3)	(4)	(5)
H_2(0-0)S(8) [a]	5.053	2.33±0.08	2.1±0.7	4.2±0.07
[FeII] [b]	5.340	10.4±0.3	11±2	20.9±0.6
[FeVIII] [b]	5.447	7.9±0.4		11±1
[MgVII] [b]	5.503	12.4±0.3		13±2
H_2(0-0)S(7) [a]	5.511	7.7±0.6	7.0±0.4	12±2
[MgV] [b]	5.610	16.2±0.4		20.1±0.6
[KIV] [a]	5.982	1.0±0.2		1.0±0.1
H_2(0-0)S(6) [a]	6.109	4.0±0.2	1.6±0.4	6.5±0.2
[SiVII] [a]	6.492	0.9±0.2		0.7±0.2
[NiII] [a]	6.636	1.4±0.3		
H_2(0-0)S(5) [a]	6.910	16.6±0.5	6.6±0.2	29.4±0.4
[ArII] [b]	6.985	43.0±0.9	5.7±0.3	59±1
[NaIII] [a]	7.318	3.1±0.2		3.7±0.3
Pfund-α [a]	7.460	2.7±0.2		3.9±0.1
[NeVI] [b]	7.652	70±2	0.6±0.07	77±2
[FeVII] [b]	7.815	5.9±0.8		6.9±0.8
[ArV] [b]	7.902	3.3±0.2		4.3±0.4
H_2(0-0)S(4) [a]	8.025	8.3±0.2	2.1±0.1	14.2±0.2
[ArIII] [b]	8.991	22.2±0.5	1.2±0.2	27.6±0.6
[FeVII] [b]	9.527	7.8±0.4		8.1±0.5
H_2(0-0)S(3) [a]	9.66	14.3±0.3	5.7±0.2	27.0±0.4
[SIV] [b]	10.51	52±1	6.1±0.4	65±2
H_2(0-0)S(2) [a]	12.28	11.0±0.4	4.1±0.1	16.5±0.3
[NeII] [b]	12.81	143±3	11.3±0.3	160±4
[NeV] [b]	14.32	59±2	3.5±0.2	63±2
[NeIII] [b]	15.56	158±2	11.3±0.2	169±3
H_2(0-0)S(1) [a]	17.03	22.6±0.6	8.6±0.2	31.3±0.2
[SIII] [b]	18.71	67±1	7.2±0.3	73±2
[NeV] [b]	24.32	34±3	3.7±0.5	35±2
[OIV] [b]	25.89	149±5	18±1	155±5

Notes. Columns describe the: (1) name of each detected emission line, (2) central wavelength from lab of each emission line, and (3,4,5) measured flux in the nuclear, circumnuclear, and central spectra, respectively. [a]Line fit with one Gaussian component. [b]Line fit with two Gaussian components. Nuclear region covers a circular area centred on the nucleus of the source and with a radius equal to 1.5 × FWHM(λ), where FWHM(λ) = 0.17 kpc for λ < 8 μm and FWHM(λ) = 0.17 × λ[μm]/8 kpc for λ > 8 μm. Circumnuclear region covers an annulus area centred on the nucleus of the source, and with an inner radius of 0.55 kpc and an outer radius of 0.88 kpc. Central region covers a circular area centred on the nucleus of the source and with a radius of 0.88 kpc. Additional uncertainties in the absolute flux of 10% for all channels should be considered.

continuum surrounding the emission line. This noise was used to generate new spectra (n = 500), where a random Gaussian noise with a sigma equal to the rms was added to the original spectrum before the lines were fitted again. The final uncertainty is the standard deviation of the n individual measurements. Table 2 presents the fluxes of all emission lines detected in the nuclear, circumnuclear, and central spectra of NGC 6552. The central wavelengths of the systemic components of all emission lines detected in the nuclear spectra give a median redshift of 0.0267±0.0002, in agreement with previous estimates (Paturel et al. 2002). We found that the current MRS wavelength calibration is, in general, better than the FWHM of the MRS line spread function (LSF, Labiano et al. 2021; Jones et al. 2023).

All the emission lines in the NGC 6552 spectra are spectrally resolved. Molecular hydrogen lines present one-component Gaussian profiles, with intrinsic line FWHMs of 312±34 km s^{-1}. In contrast, the high S/N atomic forbidden lines (high- or low-excitation ones) have asymmetric profiles, with blue wings. Pfund-α, the only hydrogen atomic line detected in the NGC 6552 spectra, presents an intrinsic line FWHM of 442±22 km s^{-1}, greater than the average widths of the atomic forbidden and molecular hydrogen lines, and with no evidence of asymmetries.

The atomic lines show a combination of systemic and a blue-shifted velocity components and we characterised them by a two-component Gaussian fit. Figure 5 illustrates the analyses of high-excitation and coronal atomic lines ($E^*_{ion} \gtrsim 30$ eV). We found that the systemic and blue-shifted velocity components of these emission lines are consistent within the given error bars, independent of their ionisation potentials or critical densities. The average systemic line FWHM, 270±50 km s^{-1}, agrees with the one of the molecular hydrogen lines. The blue-shifted velocity components are not spatially resolved in the MRS observations, suggesting that they are fully localised in the nucleus of the galaxy. Its physicals scales should be lower than 170 pc that corresponds to the physical scales of the MRS PSF FWHM at 5 μm. Table 3 summarises the properties of the blue-shifted velocity component, together with the ionisation potential and critical density of each high-excitation atomic line in the nuclear spectrum of NGC 6552. The blue-shifted velocity components is characterised by average velocity offsets (V_{peak}) of −127±45 km s^{-1} relative to the narrow component and with intrinsic line FWHMs of 673±123 km s^{-1}. The nuclear blue-shifted velocity component dominates the emission of the high-excitation lines with a 67±7% of the total flux of the line. Low-excitation atomic lines ($E^*_{ion} \lesssim 20$ eV, namely, [FeII], [ArII], [SIII], and [NeII]) also show the presence of a blue-shifted velocity component with similar kinematic properties, that is, V_{peak} and line FWHMs, as those identified in the high-excitation lines but carrying out only between 20% and 36% of the total flux of the line. Then, their main flux contribution is associated with the systemic velocity component that shows a slightly broader line FWHMs (354±26 km s^{-1}) than the high-excitation lines.

5.2. Highly ionised nuclear outflow. Kinematics and physical properties.

The blue-shifted velocity components identified in all atomic emission lines are interpreted as being due to the presence of outflowing material close to the AGN. This is the first clear observational evidence for a nuclear outflow in NGC 6552. The outflow share the same kinematics and fraction of the total flux in all high-excitation and coronal emission. This clearly indicates that independently of the ionisation state (from about 28 to 187 eV, see Table 3), the lines are tracing the same regions of the nuclear outflow. This is fully ionised, with no evidence of any stratification in its ionisation structure. Moreover, the outflowing gas is characterised by a blue-shifted velocity offset of −127±45 km s^{-1}, on average, with outflow maximal velocities ($V_{peak} + 2 \times \sigma_{blue}$, where σ_{blue} is the sigma of the Gaussian component fit) of 698±80 km s^{-1} (see Table 3). This implies that when assuming a bi-conical structure centred on the AGN, we are predominantly seeing the outflowing gas coming towards us. The opacity of the interstellar medium in the mid-IR is

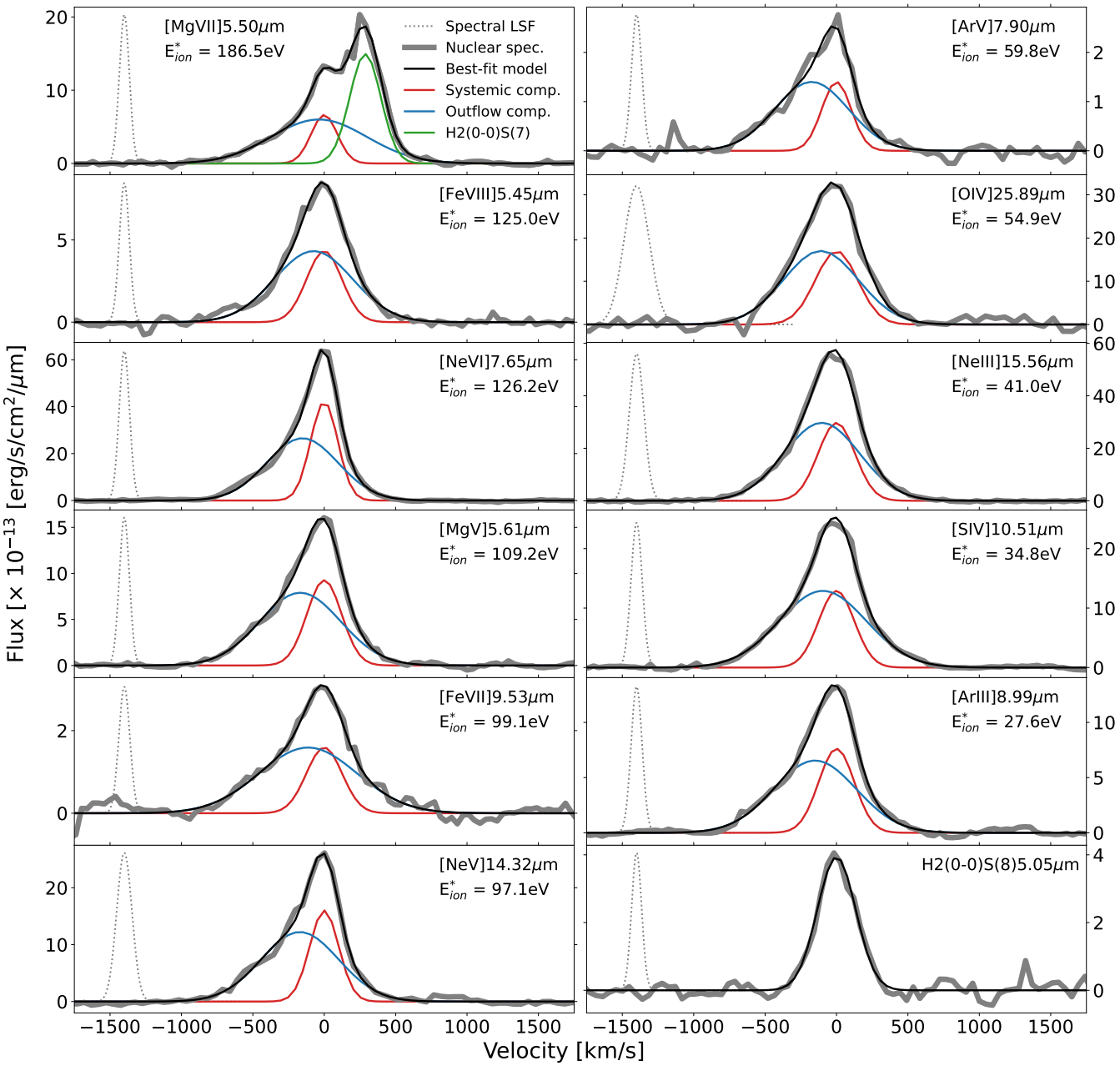

Fig. 5. Characterisation of line profiles of high-excitation and coronal emission lines in the nuclear spectrum of NGC 6552. The two-component Gaussian fit of eleven coronal emission lines covering ionisation potential from 27.6 to 186.5 eV is shown. If more than two emission lines trace the same ion (e.g., [NeV] at 14 and 24 μm), only the line with the highest spectral resolution is shown. For comparison, the bottom-right panel illustrates the one-component Gaussian fit of the H_2(0-0)S(8) hydrogen molecular line. Gray line shows the nuclear spectrum of NGC 6552. Black line is the best line-fit model. Red line is the systemic component. Blue line is the outflow component. Dotted gray line is the unresolved emission line for the corresponding wavelength. All systemic and outflow components of high-excitation and coronal emission lines are consistent independently of the ionisation potential. The molecular hydrogen lines do not present an outflow component, and its line profiles are in agreement with the systemic component of all high-excitation and coronal emission lines.

significantly smaller (factors 30–100) than that in the optical. However, for the large column densities measured towards the AGN in NGC 6552, i.e., $\log(N_H) = 24.05\,\mathrm{cm}^{-3}$ (Ricci et al. 2015), a large optical depth between 3.3 and 10 is expected in the 5–25 μm MRS spectral range (e.g., Corrales et al. 2016). Therefore the lack of a red velocity component in the emission line profile is interpreted as emitting outflowing gas moving away from us (i.e., receding direction) but obscured from our line of sight, even at these wavelengths, by the torus around the AGN and/or the dense medium in its vicinity.

The ratio of the [NeV]14.32 μm to [NeV]24.32 μm emission lines gives an estimation of the electron density in the highly ionised coronal emission gas. Independently of the unknown electron temperature, the low ratio measured in NGC 6552 (1.7±0.4, using absolute flux errors), indicates that the coronal gas is in the low density regime, that is, less than $10^{5.5}\,\mathrm{cm}^{-3}$ for temperatures less than 10^6 K (Dudik et al. 2007). However, the kinematics of the high-excitation and coronal gas ($27.6 < E^*_{\mathrm{ion}}[\mathrm{eV}] < 186.5$) are very similar, while the critical electron densities cover a wide range from $\log(n_{\mathrm{crit}}[\mathrm{cm}^{-3}])$ equal to

Table 3. Properties of the blue-shifted velocity component for all high-excitation and coronal emission lines in the nuclear spectrum of NGC 6552.

Line	λ_{lab} [μm]	E^*_{ion} [eV]	$\log(n_{crit})$ cm^{-3}	Flux [%]	FWHM [km s^{-1}]	V_{peak} [km s^{-1}]	V_{out} [km s^{-1}]
(1)	(2)	(3)	(4)	(5)	(6)	(7)	(8)
[FeVIII]	5.447	125.0	6.41	0.61 ± 0.04	637 ± 67	−88 ± 19	629 ± 61
[MgVII]	5.503	186.5	6.53	0.77 ± 0.02	786 ± 37	−36 ± 21	704 ± 25
[MgV]	5.610	109.2	6.60	0.67 ± 0.04	661 ± 22	−167 ± 12	728 ± 22
[NeVI]	7.652	126.2	5.80	0.63 ± 0.03	579 ± 20	−151 ± 10	642 ± 22
[ArV]	7.902	59.8	5.20	0.71 ± 0.07	579 ± 61	−175 ± 21	666 ± 51
[ArIII]	8.991	27.6	5.28	0.67 ± 0.03	683 ± 21	−151 ± 11	731 ± 19
[FeVII]	9.527	99.1	5.74	0.75 ± 0.02	980 ± 35	−79 ± 17	911 ± 26
[SIV]	10.51	34.8	4.75	0.70 ± 0.01	742 ± 20	−98 ± 7	727 ± 17
[NeV]	14.32	97.1	4.51	0.66 ± 0.04	606 ± 21	−175 ± 13	689 ± 23
[NeIII]	15.56	41.0	5.32	0.57 ± 0.02	652 ± 23	−117 ± 10	672 ± 19
[OIV]	25.89	54.9	4.00	0.59 ± 0.13	493 ± 102	−165 ± 75	584 ± 25

Notes. Columns describe the: (1) name of each high-excitation and coronal emission line, (2) intrinsic wavelength from lab, (3) ionisation potential, (4) critical density, (5) percentage of flux in the blue-shifted component, (6) FWHM of the blue-shifted component, (7) velocity offset relative to the narrow component, and (8) the outflow maximal velocity. [NeV]24.32 μm line profile is affected by noise and fringes, and [FeVII]7.815 μm by a spike, both of them have been discarded from the characterisation of the blue-shifted velocity component.

4–6.6 (see Fig. 5 and Table 3). This indicates that the physical conditions of the ionised gas in the outflow must be closer to the lower densities (i.e., less than a few 10^3 cm^{-3}) and temperatures (i.e., less than few 10^4 K). Otherwise, lines such as [NeV]14.3 μm and [OIV]25.9 μm would not be detected as strong as presented in the NGC 6552 nuclear spectrum (Pereira-Santaella et al. 2010). The lack of [FeII]4.89 μm emission is also consistent with low denisities (<10^3 cm^{-3} Pereira-Santaella et al. 2022).

The outflowing material appears only in the ionised gas, with no evidence of the outflow in any of the molecular rotational lines present in the nuclear spectrum. In fact, the average line FWHMs (312±34 km s^{-1}) of the molecular lines agree with the systemic velocity component of the ionised gas (270 ± 50 km s^{-1}). This could indicate that: (i) the molecular gas in the nuclear region is not directly facing the radiation coming out of the AGN and its velocity field is determined by the dynamical mass in the nuclear region or (ii) when the molecular hydrogen becomes part of the outflow, it gets quickly dissociated, contributing to wider the Pfund-α hydrogen line.

5.3. Warm molecular hydrogen

The JWST and, in particular, the MRS, will revolutionise our ability to observe the infrared lines of molecular hydrogen (Guillard et al. 2015). In NGC 6552, we detected a suite of pure rotational lines, from the brightest 0–0 S(1) 17 μm transition up to the 0–0 S(8) 5.05 μm line, at remarkable high S/N for each of the three spectral extractions (central, nuclear, and circumnuclear). Those lines arise from warm (≈100−20 000 K) molecular gas (Habart et al. 2005). We have used these observed line fluxes (Table 2) to derive the column densities and masses of warm H_2 for each of the three regions by fitting the H_2 excitation diagrams (see Wakelam et al. 2017, for a review). The statistical errors from the fits, listed in Table 2, have been added in quadrature with a 10% absolute flux uncertainty.

We emphasise that the warm (≳100 K) gas is only a fraction of the total molecular mass. Most of the cold molecular gas cannot be traced by the mid-infrared H_2 lines. If the 0–0 S(0) line at λ = 28.2 μm, which is located at the far end of the MRS-covered wavelength range and currently not properly calibrated, were available, it would provide access to the lower temperature gas and a better constraint on the total warm H_2 mass. Hence, the numbers derived here can be viewed as lower limits (see Guillard et al. 2012, for a discussion).

Figure 6 shows the excitation diagrams for the three spectral extractions, where the logarithm of the column densities of the upper H_2 levels divided by their statistical weights, $\ln(N_u/g_u)$, are plotted against their excitation energies, E_u/k_B, expressed in K. For a single uniform temperature $\ln(N_u/g_u) \propto T_{exc}^{-1}$, where T_{exc} is the excitation temperature. The plotted values of $\ln(N_u/g_u)$ have been constructed in two ways. First, in a situation of local thermal equilibrium (LTE), where the excitation temperature equals that of the gas, and where the ortho-to-para ratio (OPR) is assumed to be OPR = 3. Those values, shown as the blue circles on Fig. 6, exhibit a classical curvature, which indicates that multiple temperatures are present, and we get good agreement with a two-temperature fit that invokes a warm component (typically ≈300 K here) and a hot component (≈1200 K). We note that the spectral extraction in the nucleus shows the highest excitation. It is expected because of the stronger radiation field, and possibly stronger cosmic ray ionisation rate, or enhanced dissipation of turbulent energy close to the central nuclei (Ogle et al. 2010). The distribution of the $\ln(N_u/g_u)$ values also exhibits a 'zigzag' pattern which shows that the ortho-to-para ratio is smaller than 3 for all the regions. This indicates that the H_2 gas is thermalised to lower temperatures (Flagey et al. 2013), or that its chemistry is out of equilibrium, because the time spent hot for the gas is shorter than the ortho-to-para conversion time, as is the case in molecular shocks for instance (e.g., Neufeld et al. 1998; Wilgenbus & Cabrit 2000). We therefore constructed the excitation diagram in a second way, by fitting the OPR in addition to the two temperatures. Those column densities are displayed as the black triangles and show a smoother fit to the data. We used those fits to estimate the physical parameters of the warm H_2 gas.

The legends of each panel in Fig. 6 shows the results of the temperature and OPR fits, as well as the total column densities. Additionally, all the physical parameters derived from the fits of the excitation diagrams are gathered in Table 4. The warm H_2 masses are derived assuming an angular distance of 120 Mpc and solid angles corresponding to the extracted regions as stated

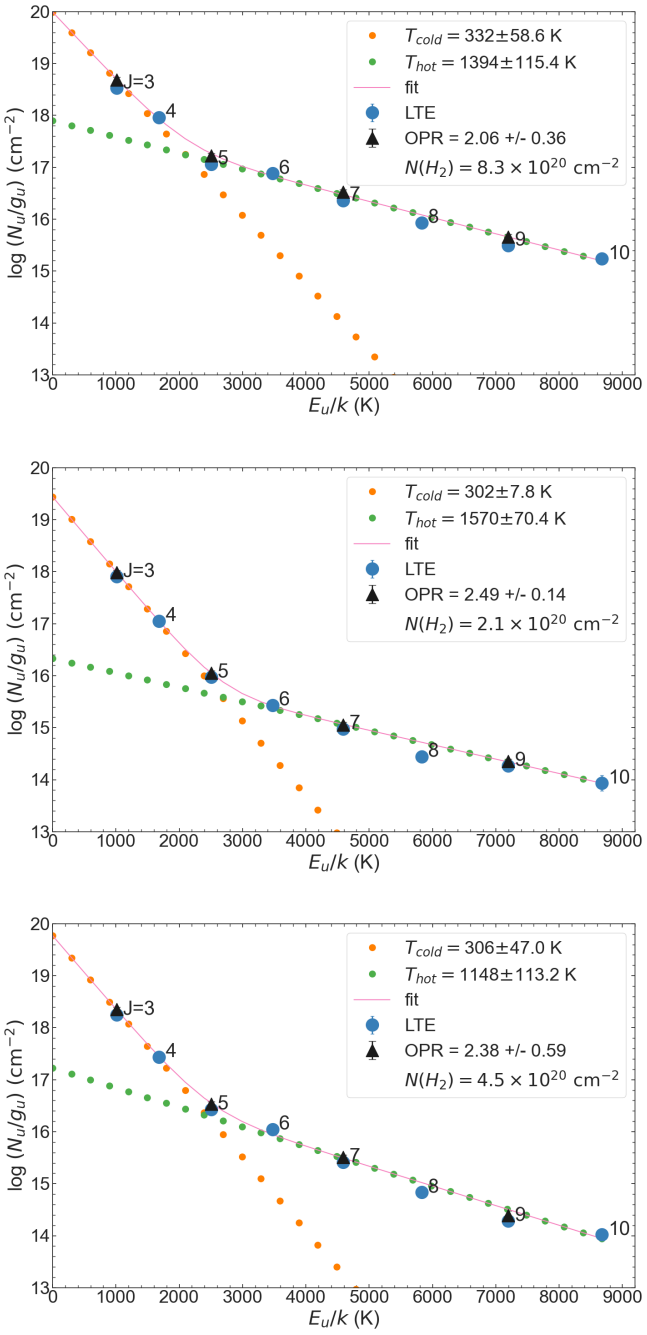

Fig. 6. NGC 6552 H_2 excitation diagrams of the three extracted regions (*top*: nucleus, *middle*: circumnuclear, and *bottom*: central). The logarithm of the column densities divided by the statistical weights of the different transitions are plotted against the upper level energies of those transitions. The LTE and fitted-OPR column densities are both displayed: the blue circles are the original column densities with LTE g_u, assuming OPR=3, while the black triangles represent the column densities calculated using the fitted OPR (see Sect. 5.3 for details). The H_2 temperatures, column densities, and masses are listed in Table 4.

in Sect. 4.2. To summarise, a mass of warm H_2 of at least $1.9 \times 10^7\ M_\odot$ is present in the central region (1.8 kpc in diameter), with almost 30% of that mass in the circum-nuclear region. The masses quoted in Table 4 are typical of what is detected at these temperatures in nearby radio galaxies or infrared galaxies (e.g., Guillard et al. 2012; Petric et al. 2018). Again, if we had access to the 0–0 S(0) line, which is sensitive to cooler gas, or if we had performed a more sophisticated modelling taking into account a distribution of temperatures, as in Togi & Smith (2016) for instance, our derived H_2 masses would be a factor 2–10 larger. We defer to a future paper the line maps fitting with detailed physical models.

Table 4. Physical parameters derived from the two-temperatures fitting of the H_2 excitation diagrams for the three spectral extractions.

Parameter		Nuclear	Circum.	Central
T(cold) [K]	(1)	332 ± 59	302 ± 8	306 ± 47
T(hot) [K]	(2)	1394 ± 115	1570 ± 70	1148 ± 113
N(cold) [10^{20} cm^{-2}]	(3)	8.0 ± 5.8	2.05 ± 0.29	4.4 ± 3.4
N(hot) [10^{19} cm^{-2}]	(4)	2.8 ± 1.1	0.08 ± 0.01	0.48 ± 0.27
N(total) [10^{20} cm^{-2}]	(5)	8.3 ± 5.8	2.1 ± 0.3	4.5 ± 3.4
Ortho-to-para ratio	(6)	2.06 ± 0.36	2.5 ± 0.2	2.38 ± 0.59
$M(H_2)$ [$10^7\ M_\odot$]	(7)	1.38 ± 0.79	0.56 ± 0.12	1.95 ± 1.13

Notes. The error bars on those parameters are calculated by propagating the uncertainties on the line fluxes, which include a 10% absolute flux calibration error and fitting errors added in quadrature. Rows describe each parameter for the nuclear, circumnuclear, and central regions. The parameters are the; (1) temperature of the cold component, (2) temperature of the hot component, (3) column density associated with the cold component, (4) column density associated with the hot component, (5) column density associated with the sum of the cold and hot component, (6) ortho-to-para ratio, and (7) total H_2 mass.

5.4. Seyfert nature of the AGN and black hole mass

The mid-IR emission lines of ionised gas have been used to disentangle the AGN and stellar emission in nearby galaxies, in particular, the sequence of different ionisation levels of neon ([NeII]12.82 µm, [NeIII]15.56 µm to [NeV]14.32,24.32 µm), and the [OIV]25.89 µm line (Pereira-Santaella et al. 2010). Table 5 shows the Neon and Oxygen line ratios for NGC 6552. They confirm that the nuclear, circumnuclear, and central spectra of NGC 6552 are close to the median values of Seyfert 1 and 2, indicating that the ionisation of the interstellar medium in NGC 6552 at distances up to a radius of 0.88 kpc from the nucleus is dominated by the AGN radiation field. However, in Sect. 4.2, we present our conclusion that channels 3 and 4 spectra of the circumnuclear region could contain up to 6% and 11% of the nuclear AGN emission, making it difficult to disentangle if the circumnuclear region is dominated by the radiation field of the AGN or star formation.

The black hole (BH) mass based on the line FWHM of the high-excitation emission line was obtained using *Spitzer* high-resolution spectroscopy in nearby galaxies (e.g., Dasyra et al. 2008). Taking the line FWHM of the systemic component in the nuclear spectrum of [NeV]14.3 µm (205±15 km s^{-1}), we derived a NGC 6552 BH mass, $\log(M_{BH}[M_\odot])$, of 6.3±0.5. This gives a mass range of 0.6–6 million solar masses, which is (on average) the mass of the Milky Way BH ($4.1 \times 10^6\ M_\odot$, Ghez et al. 2008; Event Horizon Telescope Collaboration 2022). As the MRS has a spectral resolution five times higher than the *Spitzer* high resolution mode and a sub-arcsec angular resolution at all wavelengths, the line profiles of the high-excitation and coronal lines with MIRI will provide far better and more accurate measurements of the BH mass than the initial estimates based on previous mid-IR spectroscopy.

The only hydrogen recombination line detected in the mid-IR spectral of NGC 6552 is Pfund-α with a line FWHM of 442 ± 22 km s^{-1}, which is a factor 1.5–2 larger than the ionised and

Table 5. Observed line ratios for NGC 6552 regions.

Line ratio	Nuclear	Circum.	Central
[OIV]25.89 / [NeV]24.32	4.4±1.1	4.9±1.4	4.4±1.0
[OIV]25.89 / [NeV]14.32	2.5±0.6	5.1±1.2	2.5±0.6
[NeV]24.32 / [NeV]14.32	0.6±0.2	1.1±0.3	0.6±0.2
[NeIII]15.56 / [NeV]14.32	2.7±0.6	3.2±0.7	2.7±0.6
[NeII]12.81 / [NeV]14.32	2.4±0.5	3.2±0.7	2.5±0.6
[NeIII]15.56 / [OIV]25.89	1.1±0.2	0.6±0.2	1.1±0.3
[NeII]12.81 / [OIV]25.89	1.0±0.2	0.6±0.2	1.0±0.2
[NeIII]15.56 / [NeII]12.81	1.1±0.2	1.0±0.2	1.1±0.2

molecular lines, and shows no evidence of outflowing gas. This result can be interpreted in two ways. On the one hand, the broader Pfund-α line could be tracing the inner broad line region (BLR) in this galaxy. There is already some evidence of a hidden BLR based on polarised light measurement (Tran 2001). However, the S/N of Pfund-α is not good enough to trace a very broad weak line as expected if the BLR is mostly obscured in this CT-AGN. On the other hand, the line FWHM could represent the dynamical mass of the host galaxy contained within the aperture while the width of the molecular and ionised gas would be tracing the dynamical mass in smaller regions, closer to the AGN.

6. Summary and conclusions

Galaxy NGC 6552, with an already identified Compton-thick AGN in its centre (Ricci et al. 2015), was observed with the MIRI Imager and Medium Resolution Spectrometer during the JWST commissioning to characterise the persistence of the MIRI detectors. We present the calibrated NGC 6552 MIRI image and MRS spectra, including an extensive and detailed explanation of the MIRI data and calibration process.

We obtained the nuclear, circumnuclear, and central mid-IR spectra of NGC 6552. The nuclear and central spectra are dominated by the AGN emission, with steeply rising continuum and a large number of high- and low-excitation emission lines, warm molecular Hydrogen lines, and PAH features from the interplay between the star-formation and AGN components. The spectra of the circumnuclear region is mainly dominated by the star-formation, with low excitation lines, molecular hydrogen lines, and PAH features. The central MRS spectra of NGC 6552 is consistent with previous *Spitzer* low-resolution observations and with the MIRI F560W Imager photometry.

The MIRI IFS provides the first clear observational evidence for a nuclear outflow in NGC 6552. The nuclear AGN is ionising the surrounding regions and producing a blueshifted, high-speed outflow with offset velocities of -127 ± 45 km s^{-1} and maximal velocities of 698 ± 80 km s^{-1}. The outflow is not spatially resolved (<0.2 kpc) and represents the 67±7% of the total emission of high-excitation and coronal emission lines. The analysis suggests a scenario where the outflow is fully ionised, with no evidence of stratification in its ionised structure, and produced in a low-density ($<10^3$ cm^{-3}) environment. The lack of the red component in the spectra suggests that the receding side of the outflow is obscured by material around the nucleus of the galaxy. Additionally, we confirm that NGC 6552 is a Seyfert galaxy and contains an active black hole with a low-to-intermediate mass ranging from 0.6 to 6 million $M_\odot$.

From two-temperature fits of the H_2 excitation diagrams constructed for the three regions, we derived a warm H_2 mass of at least $1.9\pm1.1\times10^7$ $M_\odot$ in the central region (1.8 kpc in diameter) of the galaxy, with 30% of that mass in the circumnuclear region (in an annulus between 0.55 and 0.88 kpc in radius). The H_2 excitation is significantly stronger in the nuclear region. The warm H_2 lines are spectrally resolved, exhibit Gaussian profiles and show no evidence of outflowing gas. The FWHM of the lines is consistent with the systemic component in the high excitation lines, suggesting that the warm molecular gas is somehow shielded from (or not aligned with) the AGN radiation and its kinematics are determined by the BH and stellar dynamical mass.

This early commissioning paper already demonstrates the huge gain in the scientific performance that JWST/MIRI provides over previous ground- and space-based infrared observatories. With respect to the study of AGNs, the high angular resolution of the MIRI IFS allows us to spatially separate the central regions of active galaxies; the high spectral resolution of MIRI enables kinematic studies that are relatively unaffected by dust extinction. Most importantly, the high sensitivity provided by the 6.5 m aperture of the JWST, offers for the first time full access to the zoo of important diagnostic lines, covering a wide range of ionisation states and offering redundant spectral information for cross-checks. Although the data for NGC 6552 are non-optimally sampled these advantages are realised and used to provide new constraints on the nature of the nucleus and circumnuclear regions. Altogether, we expect that JWST-MIRI will revolutionise the field of AGN research over the coming years.

Acknowledgements. JAM, AL, and LC acknowledge support by grant PIB2021-127718NB-100 by the Spanish Ministry of Science and Innovation/State Agency of Research MCIN/AEI/10.13039/501100011033 and by "ERDF A way of making Europe". PJK acknowledges financial support from the Science Foundation Ireland / Irish Research Pathway programme under Grant Number 21/PATH-S/9360. IA and DG thank the European Space Agency (ESA) and the Belgian Federal Science Policy Office (BELSPO) for their support in the framework of the PRODEX Programme. The work presented is the effort of the entire MIRI team and the enthusiasm within the MIRI partnership is a significant factor in its success. MIRI draws on the scientific and technical expertise of the following organisations: Ames Research Center, USA; Airbus Defence and Space, UK; CEA-Irfu, Saclay, France; Centre Spatial de Liége, Belgium; Consejo Superior de Investigaciones Científicas, Spain; Carl Zeiss Optronics, Germany; Chalmers University of Technology, Sweden; Danish Space Research Institute, Denmark; Dublin Institute for Advanced Studies, Ireland; European Space Agency, Netherlands; ETCA, Belgium; ETH Zurich, Switzerland; Goddard Space Flight Center, USA; Institute d'Astrophysique Spatiale, France; Instituto Nacional de Técnica Aeroespacial, Spain; Institute for Astronomy, Edinburgh, UK; Jet Propulsion Laboratory, USA; Laboratoire d'Astrophysique de Marseille (LAM), France; Leiden University, Netherlands; Lockheed Advanced Technology Center (USA); NOVA Opt-IR group at Dwingeloo, Netherlands; Northrop Grumman, USA; Max-Planck Institut für Astronomie (MPIA), Heidelberg, Germany; Laboratoire d'Etudes Spatiales et d'Instrumentation en Astrophysique (LESIA), France; Paul Scherrer Institut, Switzerland; Raytheon Vision Systems, USA; RUAG Aerospace, Switzerland; Rutherford Appleton Laboratory (RAL Space), UK; Space Telescope Science Institute, USA; Toegepast- Natuurwetenschappelijk Onderzoek (TNO-TPD), Netherlands; UK Astronomy Technology Centre, UK; University College London, UK; University of Amsterdam, Netherlands; University of Arizona, USA; University of Bern, Switzerland; University of Cardiff, UK; University of Cologne, Germany; University of Ghent; University of Groningen, Netherlands; University of Leicester, UK; University of Leuven, Belgium; University of Stockholm, Sweden; Utah State University, USA. A portion of this work was carried out at the Jet Propulsion Laboratory, California Institute of Technology, under a contract with the National Aeronautics and Space Administration. We would like to thank the following National and International Funding Agencies for their support of the MIRI development: NASA; ESA; Belgian Science Policy Office; Centre Nationale D'Etudes Spatiales (CNES); Danish National Space Centre; Deutsches Zentrum fur Luft-und Raumfahrt (DLR); Enterprise Ireland; Ministerio De Economiá y Competividad; Netherlands Research School for Astronomy (NOVA); Netherlands Organisation for Scientific Research (NWO); Science and Technology Facilities Council; Swiss Space Office; Swedish National Space Board; UK Space Agency. This work is based on observations made with the NASA/ESA/CSA *James Webb* Space Telescope. The data were obtained from the Mikulski Archive for Space Telescopes at the Space Telescope

Science Institute, which is operated by the Association of Universities for Research in Astronomy, Inc., under NASA contract NAS 5-03127 for JWST; and from the (https://jwst.esac.esa.int/archive/) European JWST archive (eJWST) operated by the ESDC. This research made use of Photutils, an Astropy package for detection and photometry of astronomical sources (Bradley et al. 2022).

References

Alonso-Herrero, A., Pereira-Santaella, M., Rigopoulou, D., et al. 2020, A&A, 639, A43
Álvarez-Márquez, J., Marques-Chaves, R., Colina, L., & Pérez-Fournon, I. 2021, A&A, 647, A133
Arribas, S., Colina, L., Bellocchi, E., Maiolino, R., & Villar-Martín, M. 2014, A&A, 568, A14
Bouchet, P., García-Marín, M., Lagage, P.-O., et al. 2015, PASP, 127, 612
Bower, R. G., Hasinger, G., Castander, F. J., et al. 1996, MNRAS, 281, 59
Bradley, L., Sipőcz, B., Robitaille, T., et al. 2022, https://zenodo.org/record/6825092
Bushouse, H., Eisenhamer, J., Dencheva, N., et al. 2022, https://zenodo.org/record/6984366
Corrales, L. R., García, J., Wilms, J., & Baganoff, F. 2016, MNRAS, 458, 1345
Dasyra, K. M., Ho, L. C., Armus, L., et al. 2008, ApJ, 674, L9
Davies, R. L., Förster Schreiber, N. M., Lutz, D., et al. 2020, ApJ, 894, 28
Dudik, R. P., Weingartner, J. C., Satyapal, S., et al. 2007, ApJ, 664, 71
Emonts, B. H. C., Colina, L., Piqueras-López, J., et al. 2017, A&A, 607, A116
Event Horizon Telescope Collaboration (Akiyama, K., et al.) 2022, ApJ, 930, L12
Fabian, A. C. 2012, ARA&A, 50, 455
Falco, E. E., Kurtz, M. J., Geller, M. J., et al. 1999, PASP, 111, 438
Fischer, T. C., Crenshaw, D. M., Kraemer, S. B., et al. 2011, ApJ, 727, 71
Flagey, N., Goldsmith, P. F., Lis, D. C., et al. 2013, ApJ, 762, 11
García-Bernete, I., Rigopoulou, D., Alonso-Herrero, A., et al. 2022, MNRAS, 509, 4256
Gasman, D., Argyriou, I., Sloan, G. C., et al. 2023, A&A, in press https://doi.org/10.1051/0004-6361/202245633
Gáspár, A., Rieke, G. H., Guillard, P., et al. 2021, PASP, 133, 014504
Ghez, A. M., Salim, S., Weinberg, N. N., et al. 2008, ApJ, 689, 1044
Gioia, I. M., Henry, J. P., Mullis, C. R., et al. 2003, ApJS, 149, 29
Glasse, A., Rieke, G. H., Bauwens, E., et al. 2015, PASP, 127, 686
Guillard, P., Ogle, P. M., Emonts, B. H. C., et al. 2012, ApJ, 747, 95
Guillard, P., Boulanger, F., Lehnert, M. D., Appleton, P. N., & Pineau des Forêts, G. 2015, SF2A-2015: Proceedings of the Annual meeting of the French Society of Astronomy and Astrophysics, 81
Habart, E., Walmsley, M., Verstraete, L., et al. 2005, Space. Sci. Rev., 119, 71
Harrison, F. A., Craig, W. W., Christensen, F. E., et al. 2013, ApJ, 770, 103
Harrison, C. M., Alexander, D. M., Mullaney, J. R., et al. 2016, MNRAS, 456, 1195
Jansen, F., Lumb, D., Altieri, B., et al. 2001, A&A, 365, L1
Jarrett, T. H., Cohen, M., Masci, F., et al. 2011, ApJ, 735, 112
Jones, O. C., Álvarez-Márquez, J., Sloan, G. C., et al. 2023, MNRAS, submitted [arXiv:2301.13233]
King, A., & Pounds, K. 2015, ARA&A, 53, 115
Labiano, A., Azzollini, R., Bailey, J., et al. 2016, SPIE Conf. Ser., 9910
Labiano, A., Argyriou, I., Álvarez-Márquez, J., et al. 2021, A&A, 656, A57
Markwardt, C. B. 2009, ASP Conf. Ser., 411, 251
Moran, E. C., Halpern, J. P., & Helfand, D. J. 1996, ApJS, 106, 341
Neufeld, D. A., Melnick, G. J., & Harwit, M. 1998, ApJ, 506, L75
Ogle, P., Boulanger, F., Guillard, P., et al. 2010, ApJ, 724, 1193
Paturel, G., Dubois, P., Petit, C., & Woelfel, F. 2002, LEDA
Pereira-Santaella, M., Diamond-Stanic, A. M., Alonso-Herrero, A., & Rieke, G. H. 2010, ApJ, 725, 2270
Pereira-Santaella, M., Colina, L., García-Burillo, S., et al. 2018, A&A, 616, A171
Pereira-Santaella, M., Álvarez-Márquez, J., García-Bernete, I., et al. 2022, A&A, 665, L11
Petric, A. O., Armus, L., Flagey, N., et al. 2018, AJ, 156, 295
Planck Collaboration XIII 2016, A&A, 594, A13
Ressler, M. E., Sukhatme, K. G., Franklin, B. R., et al. 2015, PASP, 127, 675
Ricci, C., Ueda, Y., Koss, M. J., et al. 2015, ApJ, 815, L13
Rieke, G. H., Ressler, M. E., Morrison, J. E., et al. 2015a, PASP, 127, 665
Rieke, G. H., Wright, G. S., Böker, T., et al. 2015b, PASP, 127, 584
Rigby, J., Perrin, M., McElwain, M., et al. 2022, PASP, submitted [arXiv:2207.05632]
Rodríguez-Ardila, A., Prieto, M. A., Viegas, S., & Gruenwald, R. 2006, ApJ, 653, 1098
Shu, X. W., Wang, J. X., Jiang, P., Fan, L. L., & Wang, T. G. 2007, ApJ, 657, 167
Spilker, J. S., Aravena, M., Phadke, K. A., et al. 2020, ApJ, 905, 86
Togi, A., & Smith, J. D. T. 2016, ApJ, 830, 18
Torres-Albà, N., Marchesi, S., Zhao, X., et al. 2021, ApJ, 922, 252
Tran, H. D. 2001, ApJ, 554, L19
Veilleux, S., Cecil, G., & Bland-Hawthorn, J. 2005, ARA&A, 43, 769
Veilleux, S., Meléndez, M., Sturm, E., et al. 2013, ApJ, 776, 27
Veilleux, S., Maiolino, R., Bolatto, A. D., & Aalto, S. 2020, A&A Rev., 28, 2
Wakelam, V., Bron, E., Cazaux, S., et al. 2017, Mol. Astrophys., 9, 1
Wells, M., Pel, J.-W., Glasse, A., et al. 2015, PASP, 127, 646
Wilgenbus, D., Cabrit, S., & Pineau des Forêts, G., & Flower, D. R., 2000, A&A, 356, 1010
Wright, E. L. 2006, PASP, 118, 1711
Wright, G. S., Wright, D., Goodson, G. B., et al. 2015, PASP, 127, 595